JGR Oceans

RESEARCH ARTICLE
10.1029/2021JC018336

Diagnosing Frontal Dynamics From Observations Using a Variational Approach

Eugenio Cutolo[1], Ananda Pascual[1], Simón Ruiz[1], T. M. Shaun Johnston[2], Mara Freilich[3], Amala Mahadevan[3], Andrey Shcherbina[4], Pierre-Marie Poulain[5], Tamay Ozgokmen[6], Luca R. Centurioni[2], Daniel L. Rudnick[2], and Eric D'Asaro[4]

[1]IMEDEA (CSIC-UIB), Esporles, Spain, [2]Scripps Institution of Oceanography, La Jolla, CA, USA, [3]Woods Hole Oceanographic Institution, Woods Hole, MA, USA, [4]Applied Physics Laboratory, Seattle, WA, USA, [5]NATO, La Spezia, Italy, [6]University of Miami, Miami, FL, USA

Abstract Intensive hydrographic and horizontal velocity measurements collected in the Alboran Sea enabled us to diagnose the three-dimensional dynamics of a frontal system. The sampled domain was characterized by a 40 km diameter anticyclonic eddy, with an intense front on its eastern side, separating the Atlantic and Mediterranean waters. Here, we implemented a multi-variate variational analysis (VA) to reconstruct the hydrographic fields, combining the 1-km horizontal resolution of the Underway Conductivity-Temperature-Depth (CTD) system with information on the flow shape from the Acoustic Doppler Current Profiler velocities. One advantage of the VA is given by the physical constraint, which preserves fine-scale gradients better than the classical optimal interpolation (OI). A comparison between real drifter trajectories and virtual particles advected in the mapping quantified the improvements in the VA over the OI, with a 15% larger skill score. Quasi-geostrophic (QG) and semi-geostrophic (SG) omega equations enabled us to estimate the vertical velocity (w) which reached 40 m/day on the dense side of the front. How nutrients and other passive tracers leave the mixed-layer and subduct is estimated with 3D advection from the VA, which agreed with biological sampling from traditional CTD casts at two eddy locations. Downwelling warm filaments are further evidence of subduction, in line with the w from SG, but not with QG. SG better accounted for the along-isopycnal component of w in agreement with another analysis made on isopycnal coordinates. The multi-platform approach of this work and the use of variational methods improved the characterization and understanding of (sub)-mesoscale frontal dynamics.

Plain Language Summary Ocean water currents move mainly horizontally, while the vertical velocity is pretty slow and thus hard to measure. However, despite its small magnitude, vertical exchange from the ocean surface to its interior is relevant for climate change (e.g., carbon distribution and export) and contaminant dispersal. In this work, we first reconstruct the small features of the ocean combining the measurements of the water velocity with its hydrographic properties like salinity and temperature. From this reconstruction we estimated and characterized the vertical velocity in a frontal region. This estimation was possible through repetitive measurements carried on by a research vessel in the Alboran Sea and led to a magnitude of 40 m/day. We confirmed our estimations with independent observations of drifting buoys and nutrients sampling which followed 2D and 3D trajectories in agreement with our velocity fields.

Key Points:

- Combining velocity and hydrographic observations with a thermal-wind based constraint, variational analysis reconstructs small-scale frontal features
- Frontal vertical velocity computed through semi-geostrophy reaches 35 m/day and explains the subduction of nutrients and warm water filaments
- Along-isopycnal component of the vertical velocity explains 60% of its total magnitude at the front

Correspondence to:
E. Cutolo,
e.cutolo@imedea.uib-csic.es

Citation:
Cutolo, E., Pascual, A., Ruiz, S., Shaun Johnston, T. M., Freilich, M., Mahadevan, A., et al. (2022). Diagnosing frontal dynamics from observations using a variational approach. *Journal of Geophysical Research: Oceans*, *127*, e2021JC018336. https://doi.org/10.1029/2021JC018336

Received 15 DEC 2021
Accepted 15 SEP 2022

Author Contributions:
Conceptualization: Eugenio Cutolo, T. M. Shaun Johnston, Mara Freilich, Andrey Shcherbina
Data curation: Simón Ruiz, Pierre-Marie Poulain, Tamay Ozgokmen, Luca R. Centurioni
Formal analysis: Eugenio Cutolo, T. M. Shaun Johnston, Mara Freilich
Funding acquisition: Ananda Pascual, Simón Ruiz, T. M. Shaun Johnston, Amala Mahadevan, Daniel L. Rudnick, Eric D'Asaro
Investigation: Eugenio Cutolo, Ananda Pascual, T. M. Shaun Johnston, Mara Freilich
Methodology: Eugenio Cutolo, T. M. Shaun Johnston, Mara Freilich, Andrey Shcherbina

1. Introduction

Inferring the full three-dimensional (3D) dynamics of structures belonging to the meso- and submesoscale is still challenging for both in situ and remote observations. A significant improvement in satellite altimetry is expected thanks to the upcoming Surface Water and Ocean Topography (SWOT) mission (Morrow et al., 2019). Through geostrophy, horizontal velocities can be easily estimated by computing the gradients of the sea surface height or the dynamic height (Le Traon & Morrow, 2001). Additional derivations are needed to determine the vertical velocity, w. Despite their small magnitude, vertical exchanges have a fundamental contribution to air-sea interactions and carbon sequestration through the physical carbon pump (Iudicone et al., 2011). Furthermore, the vertical transport of tracers is essential from a biogeochemical perspective. Since direct measurements of w are limited and require specialized instrumentation (D'Asaro, 2003), the commonly accepted procedure is to compute it through an indirect diagnostic.

Project Administration: Ananda Pascual, Simón Ruiz, Amala Mahadevan, Tamay Ozgokmen, Daniel L. Rudnick, Eric D'Asaro
Resources: Ananda Pascual, Simón Ruiz, T. M. Shaun Johnston, Amala Mahadevan, Pierre-Marie Poulain
Software: Eugenio Cutolo
Supervision: Ananda Pascual, Simón Ruiz, T. M. Shaun Johnston, Amala Mahadevan, Tamay Ozgokmen, Daniel L. Rudnick, Eric D'Asaro
Validation: Eugenio Cutolo
Visualization: Ananda Pascual, Simón Ruiz
Writing – original draft: Eugenio Cutolo, Simón Ruiz, T. M. Shaun Johnston, Mara Freilich, Amala Mahadevan, Andrey Shcherbina, Eric D'Asaro
Writing – review & editing: Eugenio Cutolo, Ananda Pascual, Simón Ruiz, T. M. Shaun Johnston, Mara Freilich, Amala Mahadevan, Andrey Shcherbina, Pierre-Marie Poulain, Tamay Ozgokmen, Eric D'Asaro

In the quasi-geostrophic (QG) framework, assuming the conservation of potential vorticity (PV) along the geostrophic flow trajectories, w can be computed through an omega equation Hoskins et al. (1978). Semi-geostrophy (SG) offers a different approximation, which is less popular due to various analytical problems in its solution which involve coordinate changes. Including the ageostrophic effects in buoyancy advection, SG allows for a better representation of frontogenesis. Hoskins et al. (1978) developed another omega equation within this framework. More recently, Viudez and Dritschel (2004) rearranged the SG omega equations and provided examples of its limitations and benefits. All these approximations are aimed at computing the total w purely through geostrophic velocities and rely on hydrographic data. In Freilich and Mahadevan (2019) instead, starting with total horizontal velocities from numerical simulations, w is estimated in its two components: w_{uplift} and w_{iso}. The first is responsible for the isopycnal uplift, while the latter explains the vertical movements along sloping isopycnals. These two components are particularly interesting when studying water masses on an isopycnal surface, where the temperature (or salinity) can be used as a tracer to reveal horizontal and vertical transport (other authors refer to this tracer as the spice of the water masses Johnston et al. (2011); Wang and Luo (2020)).

At fronts, w and vertical transport are often stronger as seen from numerical (Klein & Lapeyre, 2009; Mahadevan & Tandon, 2006; McWilliams, 2019) and in situ experiments (Pascual et al., 2017; Ruiz et al., 2009). In the western Mediterranean Sea, specifically in the Alboran basin, several studies have reported a strong vertical velocity of up 50 m/day (Gomis et al., 2001; Rudnick et al., 2022; Ruiz et al., 2019; Tintoré et al., 1991; Zarokanellos et al., 2022). This region is an ideal site due to the almost permanent front between the Atlantic Water (AW) flowing into the Mediterranean Sea and the old recirculating Modified Atlantic Water (MAW) that intrudes southwestward along the Spanish coast. This work continues the efforts made to understand processes affecting w in the Alboran Sea. We worked within the framework of the Coherent Lagrangian Pathways from the Surface Ocean to the Interior (CALYPSO) project (Mahadevan et al., 2020), which aims to unravel how tracers and drifting objects are transported out of the mixed layer.

Here, we aim to improve the diagnosis of meso- and fine-scale w based on observations from 1 to 3 April 2019. Four parallel transects revealed an anticyclonic eddy with a 20 km radius and a salinity front on its eastern side. Temperature (T) and salinity (S) measurements were made with the Underway Conductivity Temperature Depth system (UCTD) (Rudnick & Klinke, 2007), while the shipboard Acoustic Doppler Current Profiler (ADCP) provided the total horizontal velocities. We developed a 3D multi-variate analysis (VA) based on DIVAnd (Barth et al., 2014) to objectively reconstruct the structure of the eddy and salinity front. This method aims to impove on the classical Optimal Interpolation (OI), by preserving the gradients as much as possible. Excessive smoothing leads to small magnitudes when computing w with the QG and SG approximations mentioned above. Here, we focus on the SG framework since, according to Gent et al. (1994), our scenario lies in what they call a strongly curved front where the ratio between the cross-front to along-front horizontal velocities is comparably small for an order one distance in the along front direction. Finally, although the field mapping might suggest a Eulerian approach, we also used a Lagrangian perspective, studying virtual particle advection in order to compare with our reconstructions. Reconstructions are the output fields of the different interpolation methods.

The data are described in Section 2. Section 3 describes our reconstruction techniques and details their differences. Section 4 shows the results for horizontal and vertical velocities. The discussion analyzes the benefits of the VA in the eddy context and focuses on the vertical velocity (Section 5). The latter topic, an isopycnal analysis, and advection of the virtual particles leads us to the conclusion reported in Section 6.

2. Data

Our starting data was composed mainly by satellite altimetry and chlorophyll images that were used to design the campaign and to confirm our finding of a 40-km diameter anticyclonic eddy near the Spanish coast (Figure 1). We collected the UCTD and ADCP data over 30 hr from 1 to 3 April 2019, during the leg 1 of a cruise on the R/V *Pourquoi Pas?* Most of the drifters were deployed on leg 2 after 4 April 2019 (Figure 2). The AW on the west and the MAW in the east formed a strong S front on the eastern edge of the eddy. We then crossed the front with four radiator-shaped transects with 17-km spacing which cover the whole eddy. UCTD measured T and S, while a 150 kHz ADCP measured the horizontal velocity. We used Surface Velocity Program (SVP) and CARTHE surface drifters as an independent data set to validate the horizontal velocities through a skillscore and to qualitatively compare their convergence with w.

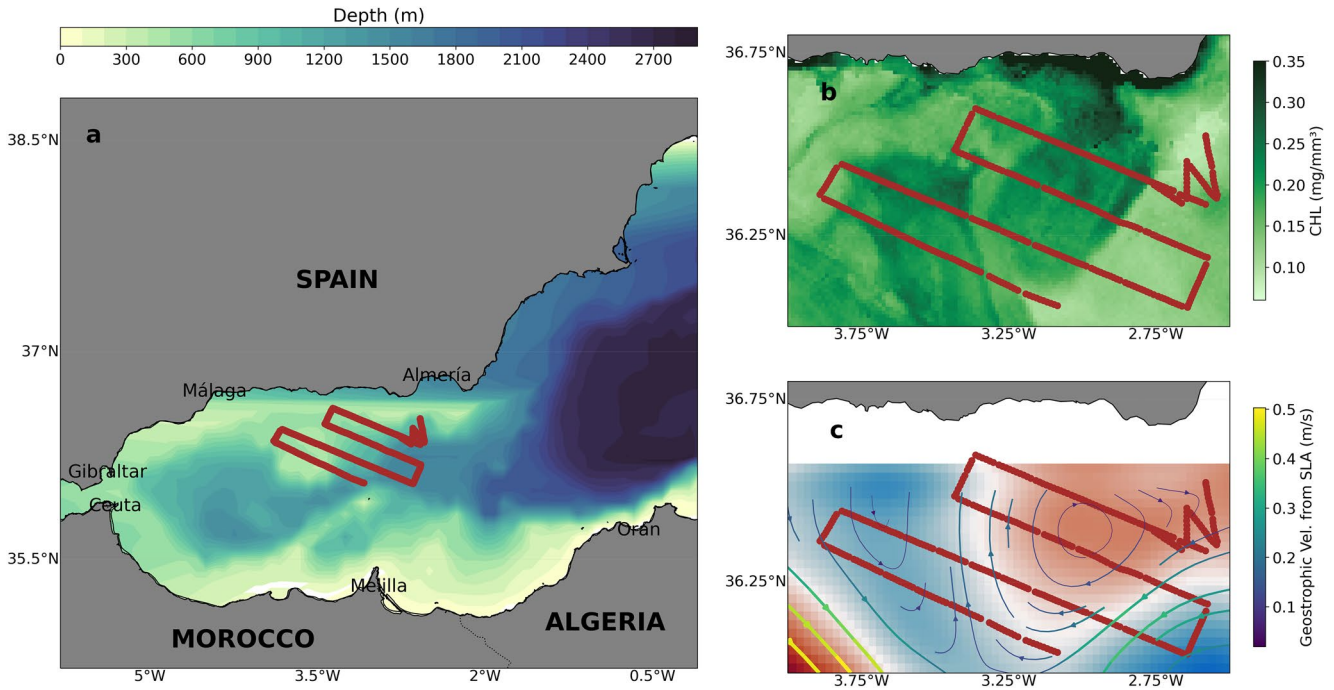

Figure 1. (a) Bathymetry of the Alboran Sea. (b) Chlorophyll image of the 1st of April 2019. (c) Sea level anomaly with geostrophic velocities of the 3rd of April 2019. Shiptrack in a contrasting color in (a, b, c).

Finally, we analyzed the 8 CTD casts made on the eddy's east side: 4 upstream and 4 downstream of the anticyclonic flow. The CTD rosette was equipped with a Sea-Bird SBE 9 CTD, a SBE 43 optical oxygen sensor, and a SUNA V2 optical nitrate sensor. Oxygen measurements were calibrated with Winkler titrations at two depths on every cast. Nitrate measurements were calibrated with water samples collected at five depths on every cast and analyzed for nitrate with a nutrient autoanalyzer at the Institute for Marine Sciences of Andalusia (ICMAN-CSIC). The nitrate and oxygen measurements were analyzed as passive tracers of the flow dynamics.

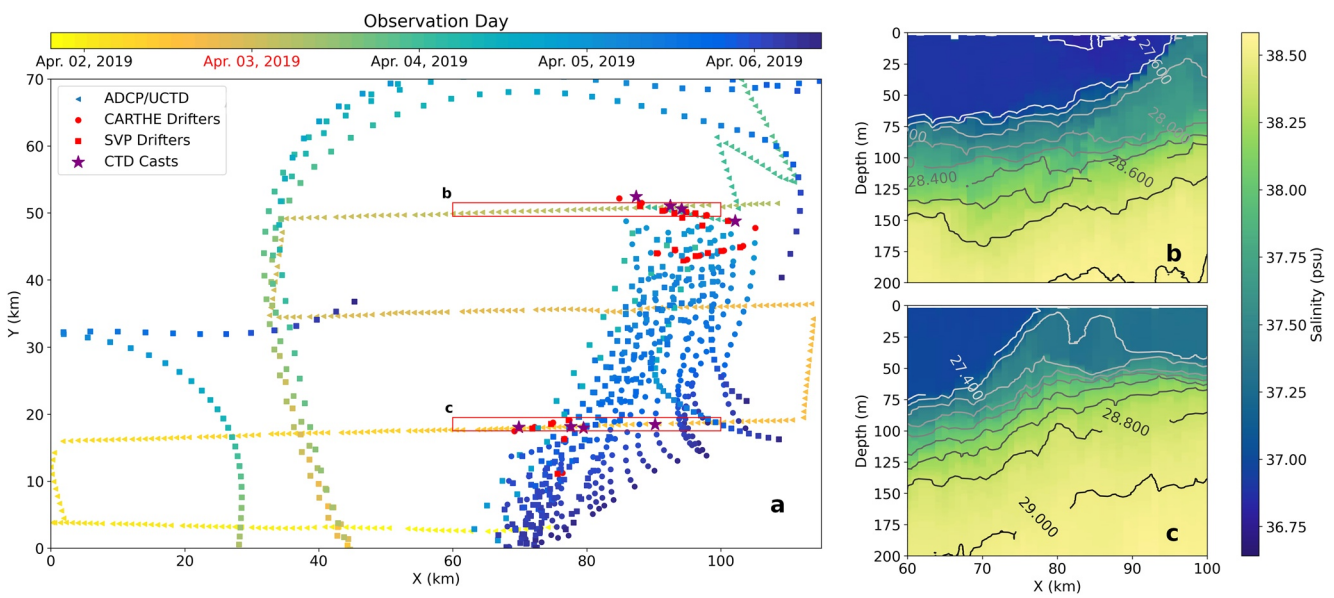

Figure 2. (a) Summary of the observations used in this work with their sampling times. The central time of the 30 hr underway conductivity temperature depth system (UCTD)/acoustic doppler current profiler sampling is highlighted with a red label. Raw observations of the salinity from the UCTD in an upstream (b) and downstream (c) section. Their position is also highlighted in the map.

We rotated the coordinates by 20° to have X correspond to the across-front direction, and Y to the along-front direction Figure 2. In X, the resolved scale is relative to the instruments' resolutions, while in Y, the separation between the transects determines the Nyquist length. Further details on this aspect and the correlation scale are in the Section Appendix A. Refer to the cruise report Mahadevan et al. (2019) for additional information on the sampling.

2.1. UCTD

The UCTD measures T, conductivity, and pressure. It consists of a compact, internally recording Sea-Bird CTD attached by Spectra line to a compact winch (Rudnick & Klinke, 2007). The UCTD was operated continuously for about 10 casts at a time without spooling line on the tail, which leads to a variable fall rate. The fall rate of the UCTD probes varied between 1.5 and 3.5 m s^{-1} and decreased at the bottom of the profiles. Data were collected at 16 Hz to 200 m. A cycle took about 5 min, which corresponds to a horizontal resolution of about 1 km, at a speed of 6 knots, resolving (sub) mesoscale features. The data were merged with the shipboard ADCP and Global Position System at times corresponding to the start of each UCTD cast. Other derived quantities such as absolute salinity, conservative temperature, and in situ density were included, once they had been computed using the Gibbs-SeaWater Package. Finally, the UCTD profiles were interpolated vertically onto a common depth grid with 0.5 m resolution.

2.2. ADCP

The broadband ADCP data were acquired with TRDI VmDAS software, which was configured for better resolution and lower noise levels: the bin size was set to 4 m, and the ambiguity velocity was set to 2 m s^{-1}. Post-processing was carried out with the University of Hawaii CODAS software, working with short time averaged file (STA) over intervals of 5 min. The complex calibration is 1.0050 ± 0.0160 for the amplitude and $-0.0060^{p}m$ 0.8533° for the phase.

The echo intensity and quality of ADCP data decreases with increasing depth. A revealing index is the percent-good (PG), that is, the percent of pings received with a noise-to-signal ratio below a certain threshold. The usual cutoff for ADCP data is $PG > 75\%$, but since the ADCP error will propagate to the UCTD reconstruction within the multivariate analysis, we use a more conservative limit $PG > 95\%$. The consequences of this choice will be discussed later.

2.3. Drifters

The drifter trajectories are independent because they are not part of the multivariate analysis. The trajectories were filtered using a lowpass Butterworth filter with a cutoff frequency of 30 hr (the inertial period is 20 hr at 36.75°N). The velocities are then obtained by differencing positions between the 2 hourly observations. Of the numerous drifters deployed during the cruise, only 44 passed through the study area: 25 Standard SVP drifters that comprise spherical surface buoy tethered to a weighted nylon drogue that tracks the horizontal motion at a nominal depth of 15 m (Niiler, 2001); 19 CARTHE drifters that are low-cost, biodegradable, and sacrificial and track currents at 40 cm below the surface. They are designed to enable large-scale deployments at an adequate spatial resolution to capture the dynamics of submesoscale features (Lodise et al., 2020). The differences between the sampling capabilities according to the sampled feature scales and the drifters drogue depths are described in Esposito et al. (2021).

3. Methods

3.1. Overview

Our goal is to reconstruct the oceanic features measured during the cruise with a particular interest in the S front on the east side. This reconstruction consists of mapping S, T, density, and velocity; using constraints to ensure consistency; and then diagnosing w with the omega equation from the mapped data. Lagrangian trajectories are derived from the 3D flow fields to explore the relationship between vertical transport and frontal configuration.

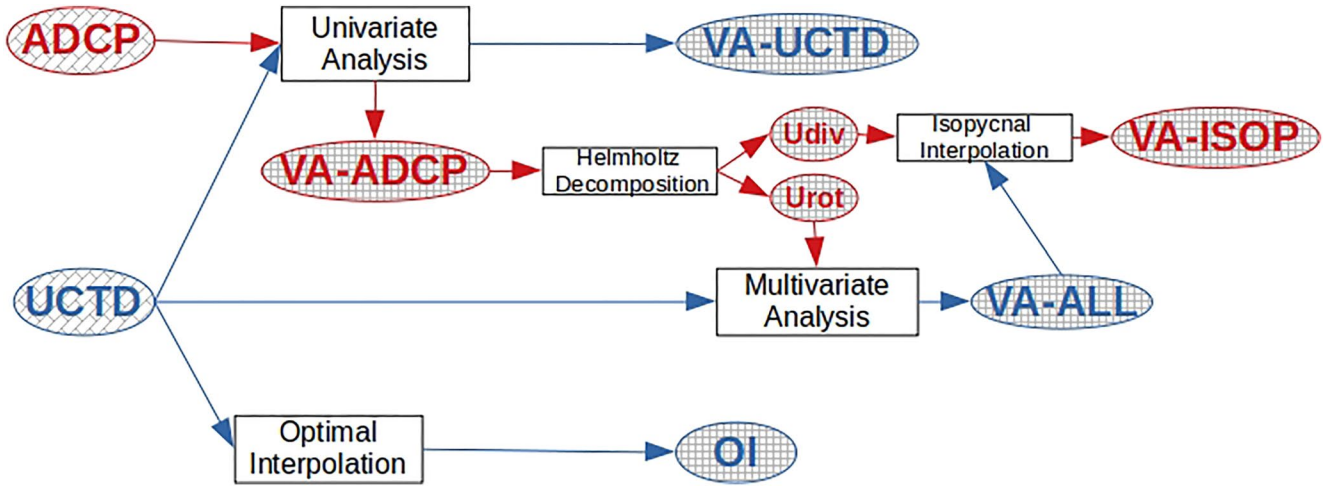

Figure 3. Reconstruction approaches tested for mapping density from the underway conductivity temperature depth system (blue) using the velocity data from the acoustic doppler current profiler (red). Udiv and Urot refer to the divergent and rotational components of the velocity from the Helmholtz decomposition (see Subsection 3.3).

To best preserve the observed ∼1-km scale cross-front variability, we investigated several mapping methods and we then applied these scales to the UCTD and ADCP measurements within a multivariate analysis. The OI method served as the baseline for comparing our mapping techniques, since it is commonly used in oceanography to obtain gridded maps from sparse observations. With this method the information from observations is distributed over the analysis domain through an a priori analytical covariance function (Donlon et al., 2012; Guinehut et al., 2002). This function can be modified for a multivariate analysis, which transforms the physical relations to statistical properties.

Here, we use a VA approach instead (Subsection 3.2), which makes use of multiple data sets in a more straightforward multivariate formulation. We distinguish between the different VA analysis with a label. The first reconstructions are univariate and use the velocity from the ADCP (VA-ADCP) and the hydrographic data from the UCTD (VA-UCTD) respectively. The main reconstruction is a multivariate one (VA-MULTI) implemented to reconstruct S and T (based on UCTD data) with a constraint involving the velocity (based on ADCP data). The CARTHE filtered drifter velocities, obtained as described in Section 2, were also used for an univariate reconstruction named VA-CARTHE. Since this mapping involves total velocity it was possible to compute the divergence in the frontal area. In fact, in this area, the CARTHE observations were sufficiently distributed in space-time to consider them synoptic, while the SVP observations were not sufficiently dense to provide a meaningful reconstruction. Univariate OI mapping is also used for the UCTD observations to provide a baseline for comparing VA-UCTD and VA-MULTI reconstructions. Since we are interested in the dynamics inferred from the different reconstructions we computed the geostrophic velocities from the density with the thermal wind relation and the vertical velocity with the omega equations from QG and SG. We tested the reconstructed horizontal and vertical velocities (Subsection 3.4) against two independent datasets: (a) the drifter trajectories which also provide information about the divergence of the flow and (b) biological sampling from the CTD. Virtual particles are advected in the reconstructed flow fields for this comparison Subsection 3.5. Finally, we map the ADCP reconstructed velocities from depth-coordinates to density levels in the VA-ISOP analysis, which enables us to estimate the along-isopycnal component of w. Figure 3 summarizes the different approaches.

3.2. Variational Analysis

The objective of VA is to map a field by minimizing a cost function, which is usually defined in terms of the deviation of the map from the observations. It is tailored to the user's needs and may include additional constraints. Different variables can be combined in a multivariate approach by adding constraints derived from physical relations. Due to these characteristics, multivariate VA lends itself well to 3D or 4D data assimilation (Dobricic & Pinardi, 2008; Rabier et al., 2000). Here, we use the VA software DIVAnd (Barth et al., 2014) to explore both the univariate and multivariate approaches. Univariate analyses are implemented for the horizontal velocity field

(either VA-ADCP or VA-CARTHE). *S*, *T*, and density are part of a further univariate analysis (VA-UCTD). The cost function *J* for these reconstructions is simply the one implemented in the software DIVAnd (Barth et al., 2014) and can be expressed for a field Γ as

$$J[\Gamma] = \sum_{n=1}^{N_o} \mu_n[\Gamma_n - \Gamma(\mathbf{x}_n)]^2 + \|\Gamma\|^2. \quad (1)$$

The first term of the RHS is the sum of the squared deviations between the reconstruction (Γ) in 3D position ($\mathbf{x}_n$) and N_o observations (Γ_n) with μ_n as their weights. These weights are the inverse of the observations' representative errors. The second term $\|\Gamma\|^2$ is the smoothing term and, as described by Barth et al. (2014), it involves a scalar product that is scaled by the different correlation lengths, symmetric and with a positive norm for all fields. This term could then define a covariance function that leads to a mathematical equivalence between OI and VA when no more terms are added to the cost function. Even considering this equivalence, VA allows a straightforward assessment of which aspects are valued as more important in the mapping: a smooth field or a strict agreement with the observations.

In theory, the observational data could be mapped in 3D and over time, however our preliminary tests did not yield meaningful results because our measurements only had good spatial coverage. We view our 3-day survey as quasi-synoptic similar to previous frontal surveys (Pallàs-Sanz et al., 2010). The observations covered an area of 120×70 km and depths up to 200 m. Further considerations regarding the assumption of synopticity are provided in Section 5 while the representative errors and correlation lengths used in our analysis are discussed in Section Appendix A.

3.3. Multivariate Interpolation Scheme

A review of different methods that combine velocity and density observations to estimate total geostrophic velocities is in Rosso et al. (2014). These methods clarify some problems with multivariate analysis, such as weighting of different types of observations. Our approach is similar to Rudnick (1996), where the ADCP velocities were used to obtain a two-dimensional (2D) velocity field that minimizes its difference from the geostrophic velocity obtained through an optimal interpolation of the density. In other words, this procedure equally weights the entire water column, unlike in other studies (Allen et al., 2001) that emphasize a certain depths. In our case, the difference in magnitude between the geostrophic velocity and the velocity is not particularly relevant and a level of no-motion can be safely assumed, as discussed later.

The direction of the flow is crucial because it shows how the front is oriented. With a constraint in our VA, we preserve the direction of the measured flow. In contrast, the gradient of the reconstructed dynamic height only provides an estimate. This constraint is especially relevant (a) between the transects where the meridional component of the flow cannot be estimated from density and (b) because even with the rotated coordinate system, the front is not perpendicular to the transects. For example, in the northern part of the domain we found the front further east (Figures 2b and 2c).

To achieve the alignment between the measured velocities and the dynamic height in a physically coherent way, we use the thermal wind:

$$-f\frac{\partial v_g}{\partial z} = g\frac{\partial \rho}{\partial x}, \quad f\frac{\partial u_g}{\partial z} = g\frac{\partial \rho}{\partial y}. \quad (2)$$

Here and in the following equations we preferred to express the derivative with lower case letter for the coordinates even if in the plots they are upper case, so $\partial/\partial x$ is the derivative in the acrossfront direction and similarly for *y*. ρ is the density, *f* is the Coriolis frequency, *g* is the gravitational acceleration, and $\mathbf{u}_g = (u_g, v_g)$ are the geostrophic velocities in the across- and alongfront directions. These latter fields in our case were approximated by the rotational component of the ADCP velocities in line with previous studies Rosso et al. (2014) and references therein. We used the Helmholtz decomposition, which splits the velocities into rotational ($\mathbf{u}_{\text{rot}}$) and divergent components ($\mathbf{u}_{\text{div}}$):

$$\mathbf{u}_{adcp} = \mathbf{u}_{rot} + \mathbf{u}_{div}. \quad (3)$$

$\mathbf{u}_{\text{rot}}$ approximates the geostrophic velocity while $\mathbf{u}_{\text{div}}$ is used as described later on. This decomposition was made on our gridded velocity field from the univariate VA (VA-ADCP) with the Python package Windspharm (Dawson, 2016). Next, we imposed the thermal wind relation by adding an extra term to the density univariate cost function which then becomes multivariate:

$$J[\rho] = \sum_{n=1}^{N_o} \mu_n [\rho_n - \rho(\mathbf{x}_n)]^2 + \|\rho\|^2 + \mu_g \left(\nabla_h \rho \cdot \frac{\partial \mathbf{u}_g}{\partial z} \right)^2. \tag{4}$$

When the thermal wind relation holds the last term on the right is zero since $\partial \mathbf{u}_g / \partial z$ results perpendicular to the horizontal gradient $\nabla_h \rho = (\partial\rho/\partial x, \partial\rho/\partial y)$ being μ_g its weight. Instead the cost function of the reconstruction increases when the density gradient is not perpendicular to the vertical shear of given geostrophic velocities. We used a scalar product instead of a squared difference to avoid a direct comparison between the magnitudes of two different types of measurements. Mainly, the constraint acts on the horizontal angles between the isopycnals and $\mathbf{u}_g$ forcing them to be small. A secondary unwanted effects of this constraint is the smoothing of ρ, however, this problem can be avoided by correctly selecting μ_g (see Section Appendix A).

Finally, it should be remarked how in order to use $\mathbf{u}_{\text{rot}}$ as $\mathbf{u}_{\text{geo}}$ and then perform the multi-variate analysis we had to interpolate it to the same depths as ρ. Before proceeding with this step, we filtered velocities in the vertical with a Butterworth lowpass filter with a cutoff at 16 m (4 times the STA bin size). Even after this step, residual ageostrophic signals cannot be excluded. However, we note that the magnitude of $\mathbf{u}_{\text{rot}}$ agrees well with that of $\mathbf{u}_g$ from VA-UCTD, which is illustrated in the results section.

3.4. Computation of QG, SG Vertical Velocity

To compute the w from our mapped ρ we first obtained $\mathbf{u}_g$ from Equation 2 then we use both the Quasi-Geostrophic and Semi-Geostrophic approximations. For QG we used the canonical omega equation in its Q-vector formulation (Hoskins et al., 1978):

$$\nabla_h \cdot \left(N^2 \nabla_h w \right) + f^2 \frac{\partial^2 w}{\partial z^2} = 2\nabla_h \cdot \mathbf{Q}, \tag{5}$$

where

$$\mathbf{Q} = \frac{g}{\rho_0} \left(\frac{\partial u_g}{\partial x}\frac{\partial \rho}{\partial x} + \frac{\partial v_g}{\partial x}\frac{\partial \rho}{\partial y}, \frac{\partial u_g}{\partial y}\frac{\partial \rho}{\partial x} + \frac{\partial v_g}{\partial y}\frac{\partial \rho}{\partial y} \right) \tag{6}$$

where N is the buoyancy frequency and ∇_h is the horizontal gradient. The QG equations hold for small Rossby numbers (Ro is the relative vorticity scaled by f Hoskins et al. (1978)). The SG framework can overcome this limitation since vorticity is advected by the total horizontal velocity, not just its geostrophic part. As already mentioned, Gent et al. (1994) suggests that the SG approximation should lead to a better order of accuracy for a strongly curved front like the one studied in this work.

The problems with SG formulations rise due to its more complex resolutions. We followed Hoskins and Draghici (1977), who proposed a coordinate change to the "geostrophic" ones:

$$\begin{aligned} x_g &= x + \frac{v_g}{f} \\ y_g &= y - \frac{u_g}{f} \\ z_g &= z \end{aligned} \tag{7}$$

within this reference system, which follows the water parcels in geostrophic motion. Then we obtain an omega equation equivalent similar to the QG one:

$$\nabla_H^2 (q_g w^*) + f^2 \frac{\partial^2 w^*}{\partial z_g^2} = 2\nabla_H \cdot \mathbf{Q}^* \tag{8}$$

where $\mathbf{Q}^*$ is given by

$$\mathbf{Q}^* \equiv \left(Q_x^*, Q_y^*\right) = \left(\frac{\partial u_g}{\partial x_g}\frac{\partial \rho}{\partial x_g} + \frac{\partial v_g}{\partial x_g}\frac{\partial \rho}{\partial y_g}, \frac{\partial u_g}{\partial y_g}\frac{\partial \rho}{\partial x_g} + \frac{\partial v_g}{\partial y_g}\frac{\partial \rho}{\partial y_g}\right)\frac{g}{\rho_0}. \tag{9}$$

q_g plays the role of a semi-geostrophic static stability and is equivalent to

$$q_g = -\frac{g}{\rho} J \frac{\partial \rho}{\partial z_g}. \tag{10}$$

Together with the vertical gradient which compose N^2 there is a contribution from the geostrophic vorticity through J, the Jacobian of the transformation Equation 7 which in fact is

$$J = 1 + \frac{1}{f}\left(\frac{\partial v_g}{\partial x} - \frac{\partial u_g}{\partial y}\right) - \frac{1}{f^2}\left(\frac{\partial u_g}{\partial y}\frac{\partial v_g}{\partial x} - \frac{\partial u_g}{\partial x}\frac{\partial v_g}{\partial y}\right) \tag{11}$$

the geostrophic vorticity appears in the first term in parenthesis. J is also used to scale the vertical velocity w*

$$w^* = \frac{w}{J} \tag{12}$$

the complexity of this methodology lies in the double coordinate change required: from normal coordinate to geostrophic and vice-versa. Mahadevan and Tandon (2006) report how this procedure was not possible in model data without losing the submesoscale features with an excessive smoothing.

In this work, we faced static and relatively small fields and we could solve Equation 8 through finite-difference on an irregular grid without any interpolation following (Liszka & Orkisz, 1980). The values of the fields in the original coordinate belong to an irregular grid when considered in the corresponding geostrophic coordinate. We could proceed this way since the coordinate changes do not lead to singularities in the denominator of the finite difference. Our approach is then similar to what is done in Viudez and Dritschel (2004) and more recently in Nardelli et al. (2018), where the SG omega equation is computed without coordinate change. We retained only the first term of Equation 11 as the second one resulted as negligible, and we solved the simplest equation Equation 8 directly in the irregular grid without the chain rule. At any case, our methodology shares the same problems of Viudez and Dritschel (2004) leading to singularities when $Ro = -1$ and consequently $J = 0$, but for the present case there was no such eventuality.

3.5. Advection of Virtual Particles

To assess how well our gridded reconstructions capture the 3D transport of passive tracers, we compare the trajectories of virtual particles with observations withheld from the reconstruction. The drifters provide trajectories and 2D patterns of surface circulation, while nutrients measured on the CTD casts can be used to trace 3D flow. We compared these independent data with virtual particles advected in our reconstructions. The drifters are compared quantitatively through a skill-score based on a 2D integration, while the nutrient concentration is treated qualitatively in a 3D assessment.

Virtual particles are advected by integrating their trajectories in time using a Runge-Kutta 4th order scheme implemented through Ocean Parcels (Delandmeter & van Sebille, 2019). This software considers our reconstructions constant in time, and advects virtual particles from their specified initial positions. To obtain comparable 2D trajectories with the drifters, we initialize particles in every position included in the drifter data set (see Subsection 2.3). Since the two types of drifters have different drogue depths we used the velocity of our reconstruction at an intermediate level of 10 m. When one of the virtual particles or its corresponding drifter leaves the domain, the particle is eliminated keeping in memory its last position for the computations while the advection continues for the remaining particles. The skill-score is defined as (Liu & Weisberg, 2011)

$$s = 1 - \sum_{t=1}^{T} d_t / l_t, \tag{13}$$

where the distance between the real and the virtual drifters at the time step t is d_t, while l_t is the total distance traveled by the real drifters at the same time step. A skill-score equal to one is optimum, meaning that the distance

between the virtual drifters and the real one is 0. According to the original definition, the metric was considered equal 0 (i.e., worst skill-score) when negative. Negative values can be preserved but in our case we removed them because they occurred infrequently. A single drifter trajectory provides different skill-scores, since we advect virtual particles from all the positions along the drifter trajectory. Not all the virtual particles remained in the domain for the same amount of time, and only those that stayed at least for 10 hr were retained. The maximum time inside the domain on the other hand is 20 hr. These time scales are smaller than those in past studies using the skill-score (Halliwell et al., 2014) mostly because these other works use more extensive domains. This metric provides a way to quantitatively evaluate the different mappings. Finally, for the 3D advection, particles were initialized below the mixed layer at the locations of the upstream CTDs. The particles were advected over 24 hr to reach the downstream CTDs.

3.6. Along Isopycnal Vertical Velocity

To better understand the flow along the front and around the eddy, we mapped different variables on isopycnals. On an isopycnal, T and S are passive tracers in the absence of mixing (Wang & Luo, 2020). First, we obtain the depths spanned by an isopycnal and then we compute the isopycnal slope ∇h. The along-isopycnal w is then (Freilich & Mahadevan, 2019):

$$w_{\text{iso}} = \mathbf{u}_{\text{div}} \cdot \nabla h + \frac{|\nabla h|^2}{1 + |\nabla h|^2} \left(\frac{\partial h}{\partial t} + \mathbf{u}_{\text{rot}} \cdot \nabla h \right), \tag{14}$$

for small isopycnal slopes, the right hand side is simplified to just the first term. We obtain $\mathbf{u}_{\text{div}}$ from VA-ADCP, using Equation 3. For use in this equation, $\mathbf{u}_{\text{div}}$ was re-interpolated to the same isopycnal coordinates as ∇h. This was done by exploiting the map between depths and isopycnals previously computed and proceeding with a simple VA.

w_{iso}, is interpolated to depth coordinates and compared with other independent estimates of w. By using $\mathbf{u}_{\text{div}}$, this procedure is independent of QG and SG assumptions. In fact, even with QG and SG computations we could compute the divergent velocities through w and the continuity equation but then $\mathbf{u}_{\text{div}}$ would not be independent. Furthermore due to the QG and SG boundary conditions, w is small at the surface, which can produce erroneous velocities on isopycnals. In a baroclinic context, this error extends to greater depths. Instead, the measurement error can be considered homogeneous in the depth range selected for $\mathbf{u}_{\text{div}}$.

4. Results

4.1. Horizontal Velocities

We obtain horizontal velocities through the geostrophic balance based on dynamic height from the OI, VA-UCTD and VA-MULTI (Figure 5). OI shows a weaker flow with a smoother contour than with VA-UCTD, where stronger velocities are seen in numerous small meanders. VA-MULTI has a similar magnitude to VA-UCTD, but the flow is straighter, especially in the frontal area. The eddy core location changes in VA-MULTI and is closer to the result we obtained for $\mathbf{u}_{\text{rot}}$ from VA-ADCP (streamline in Figure 4). In addition, the spatial averages of $\mathbf{u}_{\text{geo}}$ from VA-UCTD and $\mathbf{u}_{\text{rot}}$ from VA-ADCP agree in the upper 125 m. The number of ADCP observations with PG > 95 decreases with depth to less than the 50% at 200 m. This overall agreement lends support to our assumption of 200 m as the level of no-motion for computing $\mathbf{u}_{\text{geo}}$ as originally proposed by Viúdez et al. (1996) for this area. Furthermore, $\mathbf{u}_{\text{geo}}$ agrees in magnitude with the geostrophic velocities from satellite altimetry (Figure 1).

At the eddy's southern edge, $\mathbf{u}_{\text{rot}}$ is stronger than all the geostrophic velocities (Figures 4 and 5). This same southern region shows a strong curvature, and then, according to Ioannou et al. (2019), the cyclostrophic component may be important. Since we consider the geostrophic balance, the weaker velocity is probably due to the missing cyclostrophic contribution. This term is not particularly relevant in most of the frontal areas where we focused in this study.

$\mathbf{u}_{\text{rot}}$ allows a qualitative assessment of the geostrophic velocities, but these measurements are not independent in VA-MULTI. Therefore, we use drifter trajectories as an independent comparison. For the strongest $\mathbf{u}_{\text{rot}}$, VA-MULTI produces a higher skill-score than either OI or VA-UCTD (Figure 6). Thus, the additional constraint actually improves the reconstruction with the ADCP information. Where this signal is small, negligible effects

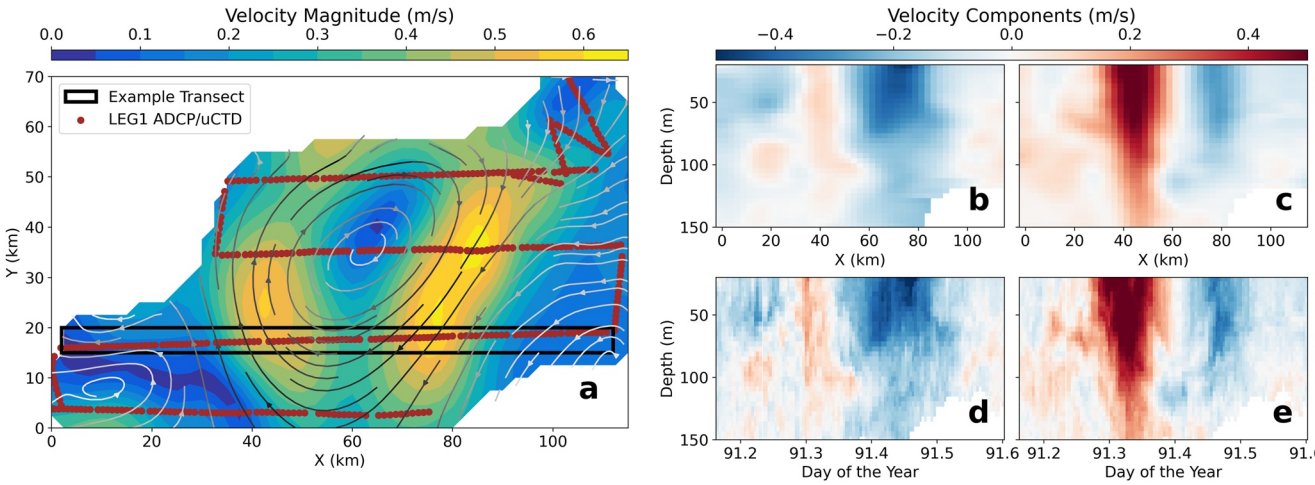

Figure 4. (a) Reconstructed horizontal velocities at 20 m depth are based on acoustic doppler current profiler (ADCP) measurements. Streamlines shows $\mathbf{u}_{rot}$. The black box shows the transect corresponding to the other panels Results of the reconstruction VA-ADCP for (b) *u* and (c) *v* are compared to measured (d) *u* and (e) *v*.

are assumed. At the front with its stronger velocities, we obtain an improvement over OI with VA-MULTI by 15%, while averaging over the whole area the increase is 5%.

Ro computed from the geostrophic velocities highlights the differences in shape between the three analyses. The most relevant difference is in the frontal region (red box; Figure 7). In VA-MULTI, the straightening and strengthening of the frontal flow leads to a clear separation between its cyclonic and anticyclonic sides. In contrast, VA-UCTD is less organized at the front. Numerous meanders of the flow show high values of both negative and positive vorticity, of up to 1.2*f*. OI again has a smoother field and smaller magnitudes by a factor of 2. The divergence is relevant and is presented in the next subsection together with *w*.

4.2. Vertical Velocity

Next, we present *w* from QG and SG from the different mapping techniques and finally w_{iso} from VA-MULTI. We focus first on the high sensitivity of *w* to the field shapes due to the higher order derivatives involved in the QG and SG omega equations. Finally, we describe the differences between these two approximations with the help of along-isopycnal mapping and Lagrangian analysis.

Figure 8 shows our results for *w* on the eddy's east side, where we found interesting frontal dynamics (red box; Figure 7). OI smooths out most of the other reconstructions' small features and its *w* magnitude is 30% smaller. The VA-UCTD shows the highest magnitude, which is probably due to artifacts (meanders described earlier). The meanders appear especially in the area between the transects and are not constrained by the data. These artificial curvatures are not present when the reconstruction is constrained by the extra data provided by the ADCP. The VA-MULTI shows greater magnitudes than OI and smaller than VA-UCTD. These results are based on the QG approximation. However, for the VA-MULTI case, the SG omega equation gives the most interesting results. We obtained a clear representation of upwelling (downwelling) on the light (dense) side of the front. In Figure 9, the convergence (divergence) computed from the VA-CARTHE mapping agrees well with the downwelling (upwelling) from the SG VA-MULTI *w* in the northern part of the domain. In contrast, in the southern part, this agreement is lost due to the lack of synopticity. As the green contours show, the northern area is reconstructed with drifter information ∼50 hr after the central day of the UCTD/ADCP sampling while the southern area relies on data taken ∼75 hr later. In these times, even considering that the usual lifespan of eddies in the Western Mediterranean is 13 days (Escudier et al., 2016) we can infer a lack of synopticity for the intense wind event occurring in these days (see Mahadevan et al. (2019)).

The improvements obtained through the SG framework on the VA-MULTI reconstruction compared to the other methods are noted in the measured *T* in two transects corresponding to the upstream and downstream CTD casts (Figure 10). *w* from SG and VA-MULTI are the only reconstructions, in which the downwelling branch of the ageostrophic circulation is co-located with a warm intrusion at the front's center in both upstream (top panel) and

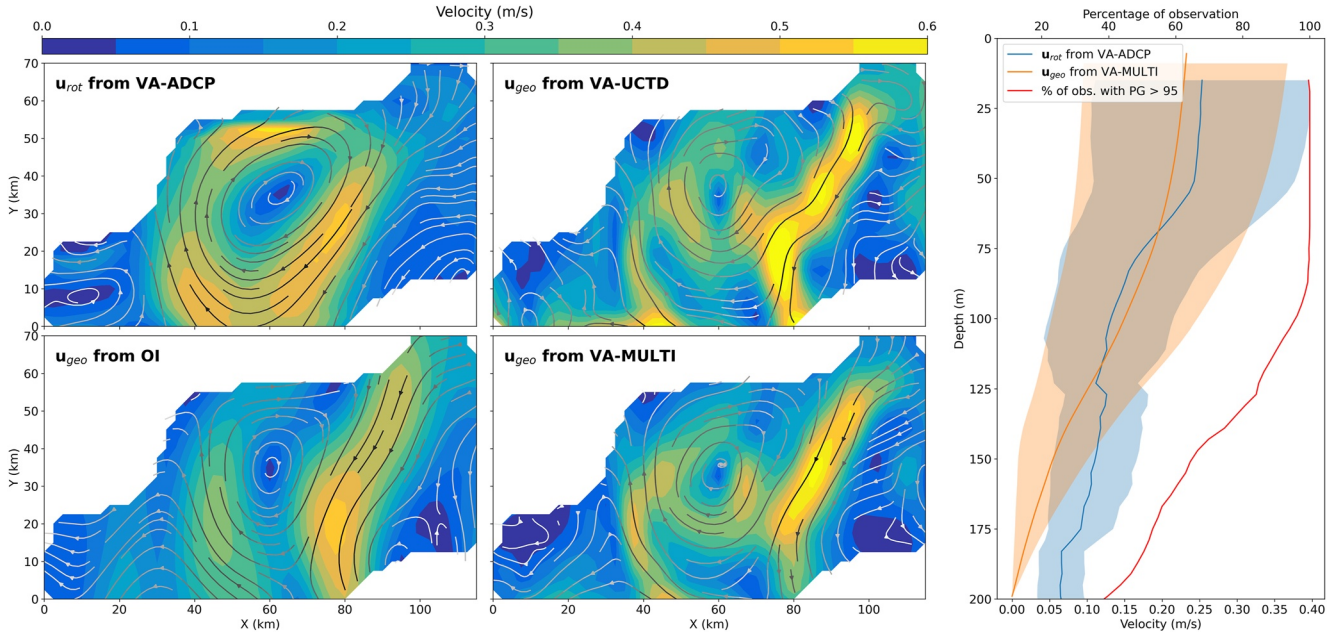

Figure 5. Surface velocity magnitudes are shown in the four panels on the left, the acoustic doppler current profiler (ADCP) panel shows $\mathbf{u}_{rot}$ while the others 3 show $\mathbf{u}_{geo}$ for the three mapping methods. In the right panel, the spatial average of the $\mathbf{u}_{rot}$ for the ADCP and u_{geo} for the VA-MULTI method are reported for the whole water column. OI and VA-UCTD averages are not reported since they present a similar magnitude to VA-MULTI. The shaded area is the spatial standard deviation. The red line is showing the percentage of observations having a PG > 95 and refers to the top scale.

downstream (bottom panel) transects (Figures 10d and 10h). Furthermore, the upstream transect also reveals the vertical structure of the w with the upwelling reaching deeper than the downwelling. The other reconstructions approach this same result except for OI, which fails in this regard. T and w are not independent since w is estimated with the omega equation from the density field. Nevertheless their coherence implies that the gradients are correctly resolved.

The isopycnal analysis helps to understand the vertical movements in the frontal region. $\mathbf{u}_{div}$ mapped on $\sigma_\theta = 28.0$ kg m^{-3} (mean depth of 70 m) shows flow converges toward the eddy's center, contributing to frontogenesis and downwelling. In particular, the flow is directed downwards where the sigma level reaches more than 100 m from a starting depth of 50 m at the front (Figure 11c). This scenario results in considerable w_{iso} at the steepest isopycnal slope on the eddy's edge (Figure 11b). w_{iso} reaches 60% of the magnitude of the total w and is particularly important in the downwelling branch of the restratification in the northeast sector of the eddy. S on this isopycnal level is a tracer in the absence of mixing and suggests a subduction process (Figure 4c).

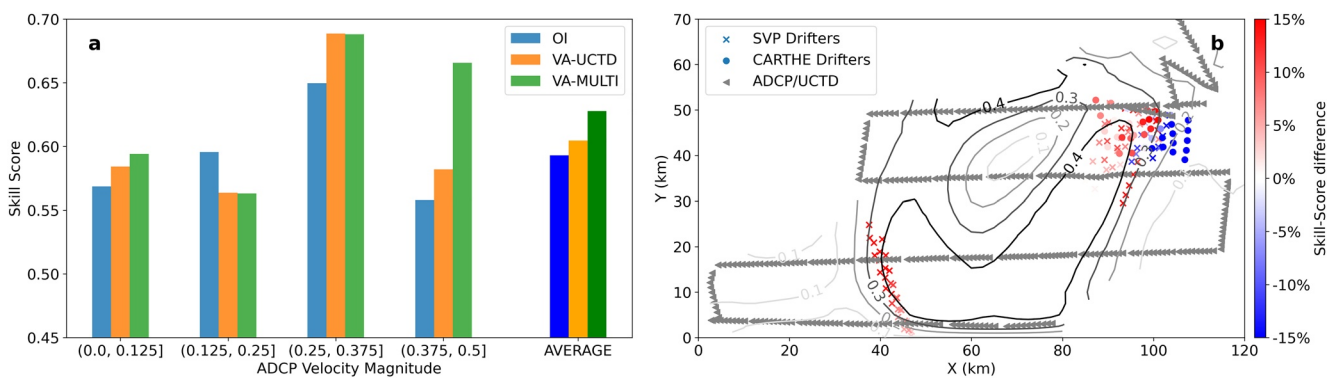

Figure 6. (a) Skill-score computed with the different reconstructions and binned by the magnitude of $\mathbf{u}_{rot}$. The last group of bars on the right shows the global average. (b) The drifters positions used with their skill-score difference (as a percentage) between the VA-MULTI and OI reconstructions. Here the contour highlights the $\mathbf{u}_{rot}$ magnitude measured in m s^{-1}.

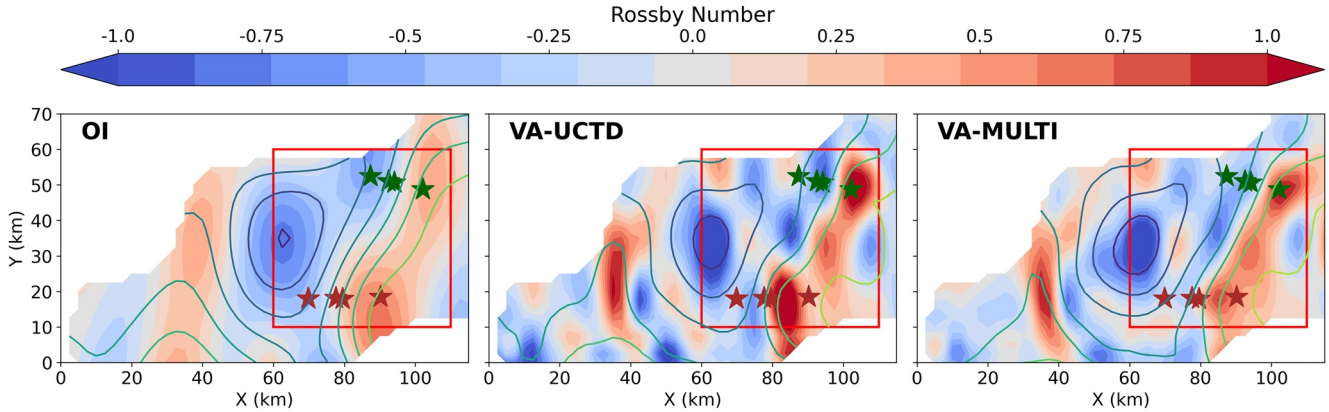

Figure 7. Rossby number (vorticity divided by *f*) for the different mapping methods, their corresponding reconstruction names are reported in the top left corner. Dynamic height contours are also shown. The green (red) stars indicate the upstream (downstream) CTD casts. The red box shows the frontal region where we analyze *w*.

The trajectories of the virtual particles advected from the upstream to the downstream CTD positions (green to brown x's; Figure 12) contribute to another description of the eddy dynamics. On the dense side (Figure 12, bottom right panel), the particles are advected from below the mixed layer and subducted with an average *w* of 15 m/day. In contrast, the particles on the light side (Figure 12, bottom left panel) are upwelled and re-enter the mixed layer, but at a deeper depth. The other particles (not shown) follow similar paths depending on their positions in the front. The higher (lower) nutrients concentration coincide with the upwelling (downwelling) region in both sides of the front. This agreement and the Lagrangian analysis is only consistent with the *w* computed with SG in VA-MULTI. Using OI, the weaker *w* led to small displacements of the particles, while with VA-UCTD, the artificial curvature led to unrealistic trajectories (not shown).

5. Discussion

In situ measurements confirmed the presence of a 40-km diameter anticyclonic eddy, initially observed in satellite altimetry and chlorophyll. The structure evolved slowly over 4 days and move eastward. Frontogenesis on that side observed with a ship-based hydrographic and biological survey. In particular, subduction takes place on the east (dense) side of the front. The drifter trajectories confirmed that the eddy maintained its shape for at least 2 days after the central day of the survey. This fact further supports the synopticity assumption of the field reconstructions.

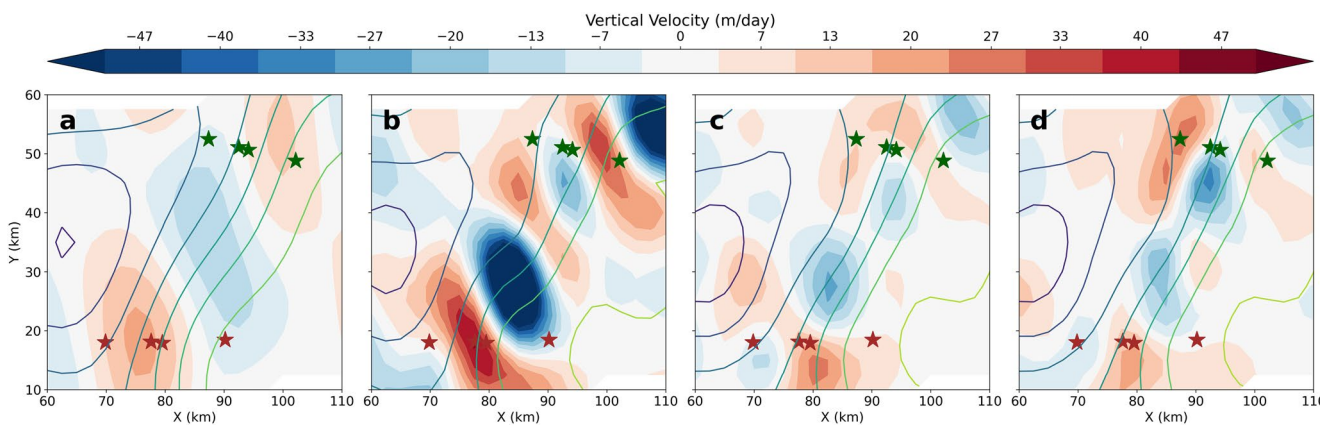

Figure 8. Vertical velocity at 50 m depth computed with different methods in the red box showed in Figure 7. The quasi-geostrophic omega equation was used on optimal interpolation, VA-underway conductivity temperature depth system and VA-MULTI reconstructions in panels a, b and c respectively. In panel d, *w* is computed with the SG omega equation in the VA-MULTI reconstruction. The green (red) stars indicate the upstream (downstream) conductivity-temperature-depth casts.

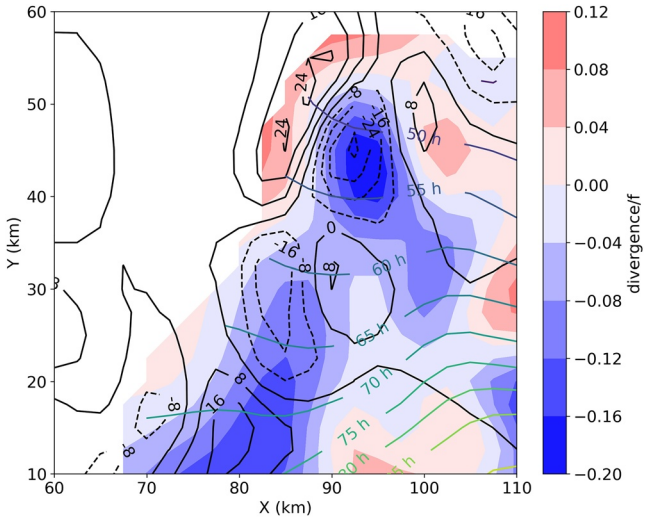

Figure 9. The surface divergence from VA-CARTHE (color). Vertical velocity (m/day) at 20-m depth from SG on the VA-MULTI reconstruction is showed with the black contour: negative (positive) values have a dashed (continuous) lines. The green contour lines indicate how many hours have passed after the central day of the underway conductivity temperature depth system/acoustic doppler current profiler sampling relative to the observations used for the mapping.

5.1. Reconstruction Methods

Considerable differences in features were found between OI, VA-UCTD, and VA-MULTI in both shapes and gradients. These differences were particularly evident when computing derivative quantities, such as the vorticity and w from the omega equation (Figures 7 and 8). Artifacts together with an unrealistic isopycnal curvature appeared in the area between the ship transects, which are (a) less constrained by the observations and (b) subject to the isotropic correlation assumed in the OI and VA-UCTD analyses. OI consistently smooths the field which results in weak magnitudes, while VA-UCTD creates an unrealistic curvature between the transects to preserve the observed gradient. We overcame these limitations with VA-MULTI. By constraining the current shear to obey the thermal wind relation, the correlation in the main flow direction preserved the anisotropic properties of the features (i.e., vertical current shear parallel to the horizontal density gradient). This was clearly visible in VA-MULTI vorticity, which presented distinct differences between the cyclonic (dense) and anticyclonic (light) sides of the front.

The independent results from the drifter analysis confirmed that VA-MULTI was the best reconstruction for both horizontal and vertical velocities. The skill-score increases up to 15% where the velocities are stronger. The extra information is thus correctly propagated to the analysis through the constraint. We did not notice any considerable difference in skill-score between the two drifter types, meaning that using the velocity field at 10 m is a good approximation for both. The VA-CARTHE mapping showed convergence in the north, in good agreement with the downwelling from VA-UCTD and

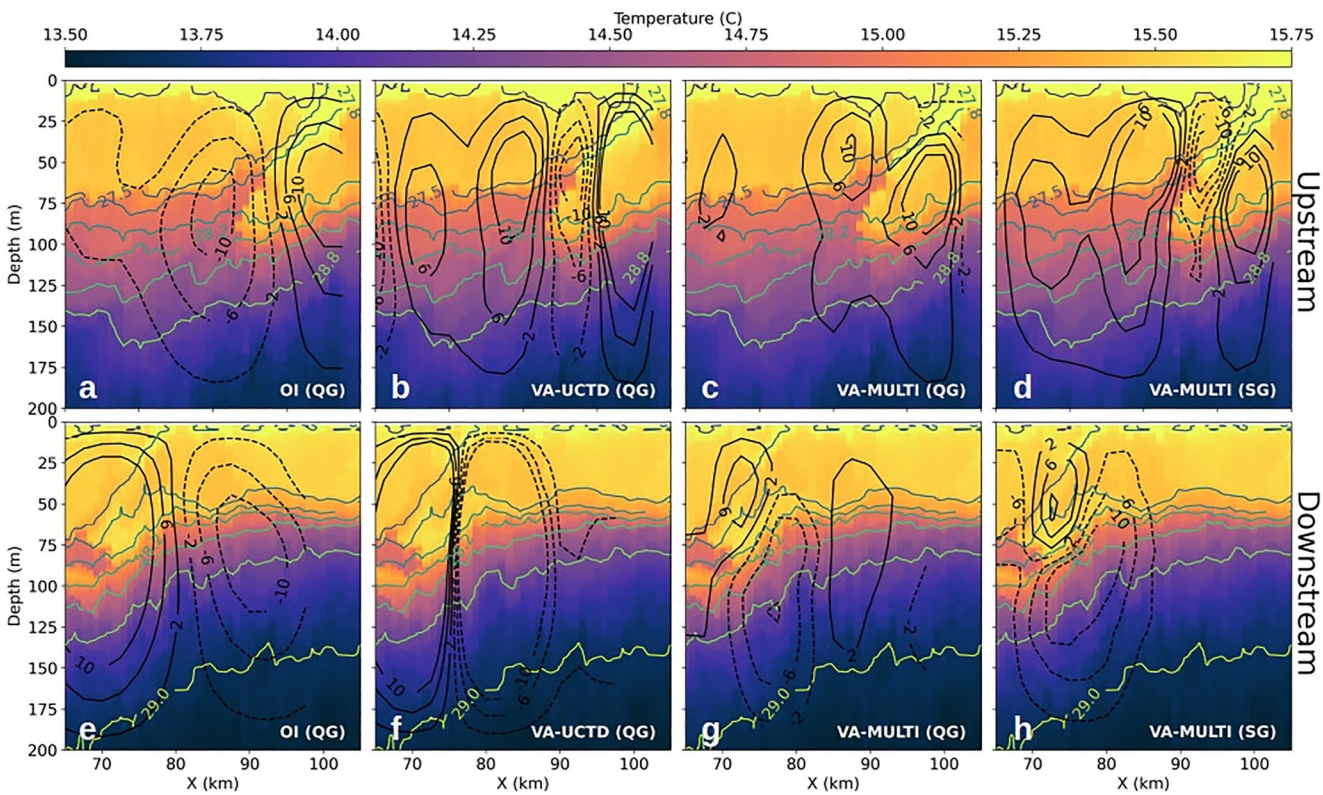

Figure 10. The top (bottom) row shows the same vertical sections of the processed but unmapped T (colors) and density (green contours) in the upstream (downstream) transect. Each column reports a different black contour for the vertical velocity corresponding to the reconstruction labeled in the bottom right corner. w is contoured in m/day with negative (positive) values as dashed (solid) lines.

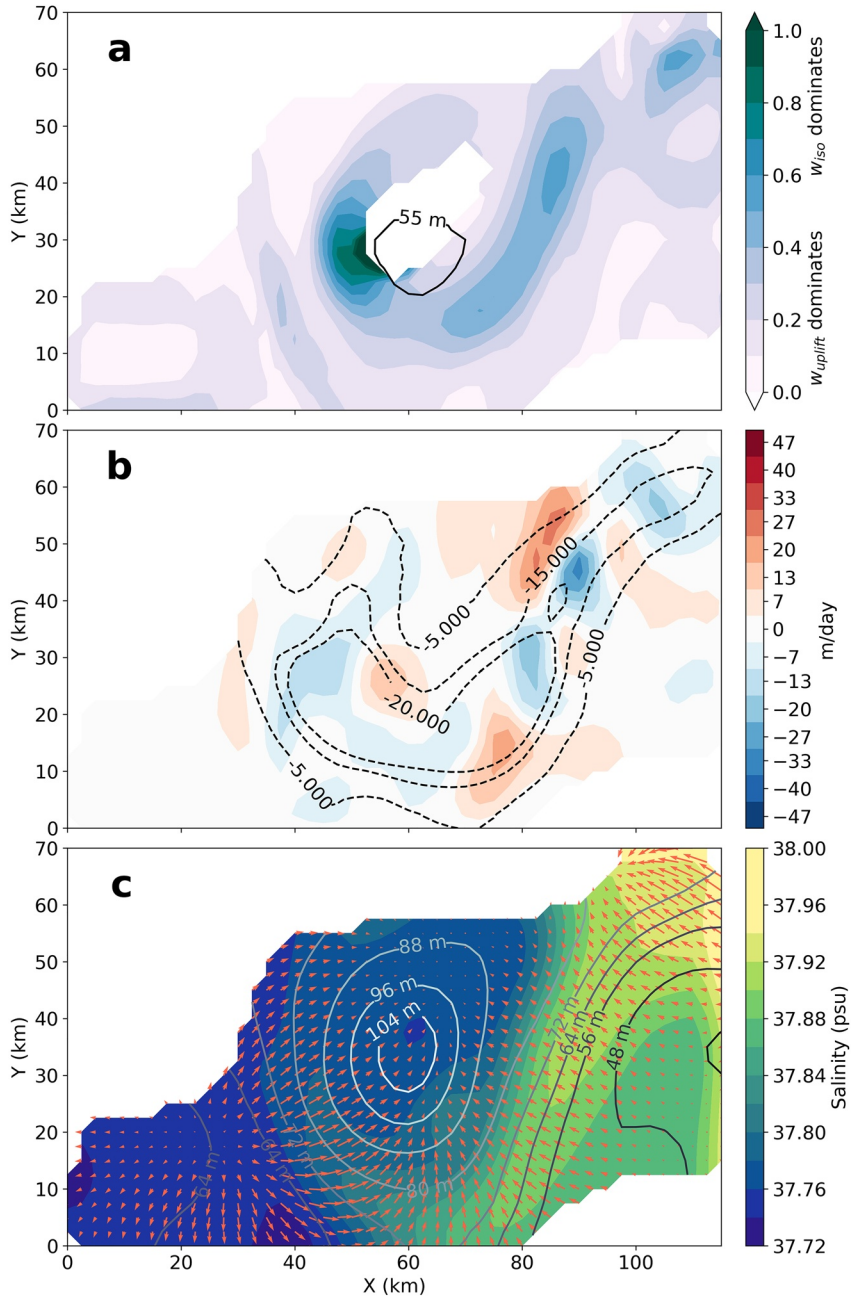

Figure 11. (a) The ratio w_{iso}/w at 50 m. The black contour shows where the mixed layer depth is below this depth. (b) The SG total vertical velocity at 50 m (colors) with w_{iso} computed with the acoustic doppler current profiler on a sigma-level and then re-interpolated to 50 m (contours). (c) Salinity on the 28.0 sigma surface shows with red vectors representing $\mathbf{u}_{div}$ and contours for the depth.

VA-MULTI (Figures 8b–8d). *w* from VA-UCTD captures the downwelling warm filament of the upstream transect (top panel in the second column of Figure 10), but does not resolve the downwelling in the downstream one (Figure 10, bottom panel). VA-MULTI benefits from the extra information especially in the south, where, due to its curvature, the front is harder to reconstruct without the velocity data.

Finally, we make some remarks on VA-MULTI cost function. The scalar product included in Equation 1 is squared and thus it constrains the gradient's direction but not its sign. This implementation is not technically problematic in the present case because the density field, even when not constrained, is almost in agreement with the

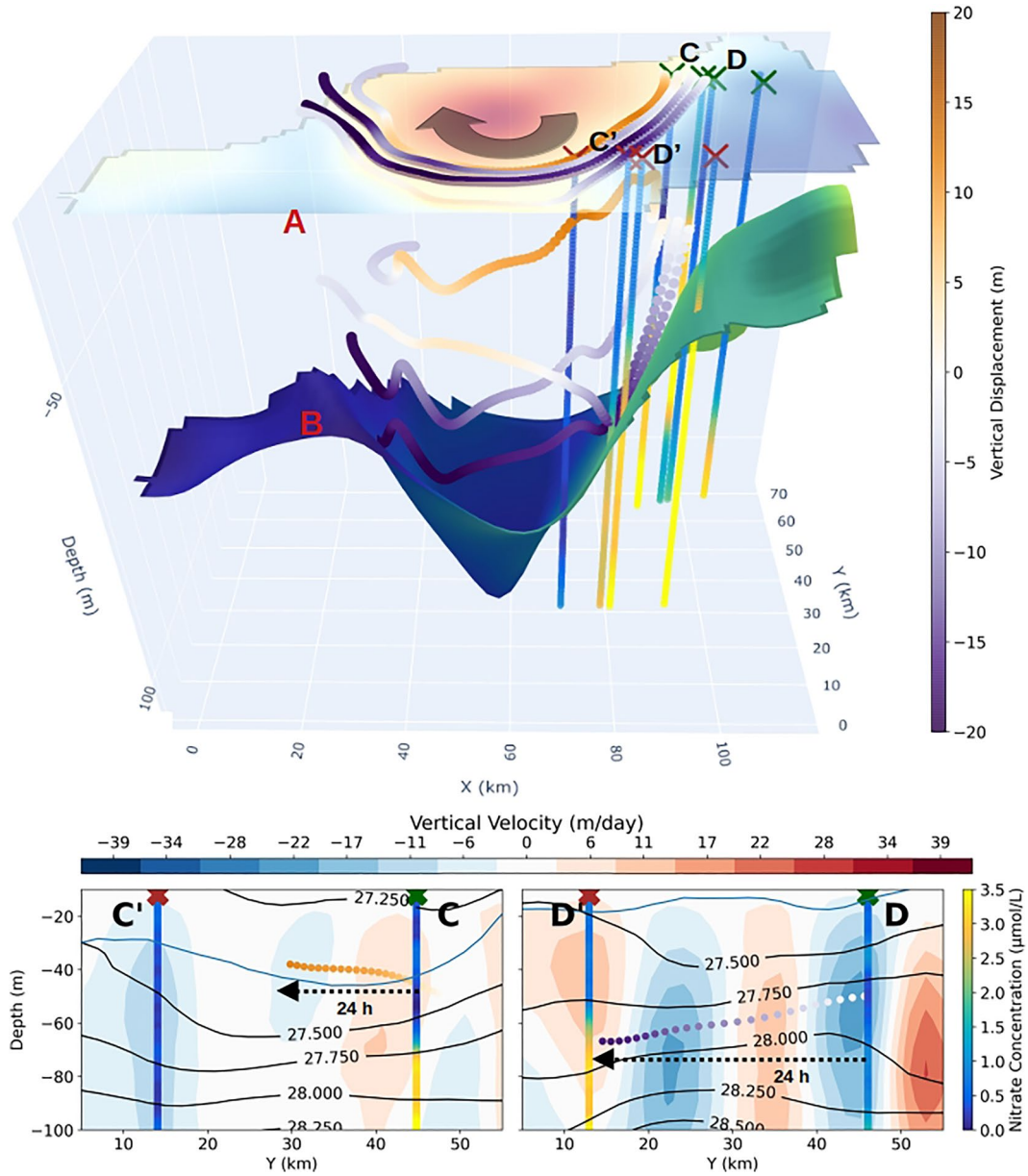

Figure 12. The larger panel on the top shows a 3D view of the eddy scenario. The 2D surface labeled with A is the dynamic height (scale not shown, red indicates higher values), B is the salinity on the 28.0 sigma surface spanning different depths (see Figure 11 c for a 2D view). The upstream (downstream) CTD cast positions are represented by green (brown) crosses. The virtual particle trajectories obtained after 5 days of advection starting from the upstream CTD casts are shown in color representing their displacement from the starting depth (see the colorbar). The 24 hr trajectories of the virtual particles going from C to C' and from D to D' are also presented in the bottom panels together with the corresponding vertical section of *w* and CTD nitrate concentrations. The black contours are the isopycnals while the blue contour is the Mixed Layer Depth.

thermal wind relation. The constraint corrects the angle between the density gradient and the geostrophic shear. In other applications, the sign of the scalar product may need to be considered in the cost function. Furthermore, we did not normalize the multivariate term, which could lead to stronger corrections of small velocities making their relative error bigger.

5.2. QG, SG and Along-Isopycnal *w*

Given that VA-MULTI better represents the horizontal dynamics assessing w leads to a better understanding of the difference between QG and SG approximations. The multi-variate constraint improves estimates of w_{iso}, which is better accounted for by SG. Isopycnals in VA-MULTI are aligned with the frontal flow and $\mathbf{u}_{div}$ is parallel to the isopycnal slope. We, therefore, obtain a considerable negative w_{iso} in agreement with the tracers.

The ageostrophic circulation computed by SG is more along isopycnal than the one computed by QG. In the upper levels of this eddy, the ageostrophic velocities point inwards, moving water masses from outside of the eddy into the interior. This is mostly an along-isopycnal process which contributes to w around the eddy edges where the isopycnals are steep. Freilich and Mahadevan (2019) reported that on average in a mesoscale eddy field, w_{iso} contributes 25% of the vertical motion. We find here that while that is consistent in an area mean, w_{iso} reached 60% of the total w on the dense side of the front. Our results confirm that the submesoscale processes are intense, and the downwelling is mostly due to the along-isopycnal component. S mapped on a sigma-level (Figure 11c) also confirms this vertical displacement occurs along an isopycnal around the eddy. In addition, the subducting filaments observed in temperature correspond better with the SG w (Figure 10). In short, the SG omega equation better estimates w_{iso} and is more appropriate in a submesoscale scenario. The comparison with the drifters' convergence (Figure 9) also suggests that the north downwelling region is correctly placed. However, a future comparison should also consider other techniques based on kinematic properties to obtain vertical velocities like in Tarry et al. (2021).

In concluding this section, we should mention that we are aware of the possible contamination of $\mathbf{u}_{div}$ by unbalanced motions. However, in our results, (a) $\mathbf{u}_{div}$ is coherent with the eddy shape with all its vectors pointing toward the center of the eddy (not shown), and (b) its magnitude is considerable at the front (about 30% of the total velocity). In comparison, barotropic tides in the area are about 5 cm s^{-1} (Pierre Poulain personal communication). Preliminary analysis based on drifters trajectories also gives similar small magnitudes of about 5 cm s^{-1} for the inertial oscillations. A remaining issue is the contribution of the internal waves. Their motion has challenged the ocean community for a long time since it is hard to separate and estimate. Some new methodology (Shakespeare et al., 2021) could help estimate this contribution in model simulations and support further uses of the divergent component of the ADCP. For the present case, since both the magnitudes and the shapes of w_{iso} are compatible with balanced motion dynamics, we were confident in presenting this analysis.

5.3. Frontal Dynamics and Nitrate Concentration

The vertical motion in the studied feature is consequential for ecology and biogeochemistry through transporting nutrients vertically through the light gradient, affecting their availability for biological production. The surface layer in the study region is depleted in nutrients due to biological uptake. The depth of the nutrient-depleted surface layer is variable within the eddy between adjacent casts in the cross-frontal direction and the along-front direction. This high variability is due to interactions between biological uptake and physical stirring and mixing. Although (Figure 12) shows that high (low) nutrient concentrations are co-located with positive (negative) w, note that the nutrient concentration is variable on a given isopycnal surface within and between transects. Therefore, to understand nutrient transport, it is necessary to account for the complex interplay between vertical advection, biological processes, and mixing in shaping biogeochemistry. Here, we provide a qualitative analysis of the frontal dynamics and nitrate concentration, focusing once again on the roles played by w_{iso} and w_{uplift}. Further analysis emphasizing the biological processes will be presented in a separate paper.

In the upstream transect, the net restratification subducts low nutrient water at cast D (in the Mediterranean water mass) while shoaling the nitracline at cast C (in the Atlantic water mass), lifting high nutrient water into the euphotic zone. There is a net downward motion from CTD cast D to cast D′. A Lagrangian particle seeded in the reconstructed velocity field at 50 m between the $\sigma = 27.75$ and $\sigma = 28.0$ surface moves from cast D to nearly the precise location of cast D′ in 24 hr while moving downwards by 20 m. While the water parcel maintains the same density, the nutrient concentration increases, and the water temperature cools (Figure 10), suggesting that the downstream increase in nutrient concentration is due to stirring and mixing of Atlantic and Mediterranean waters at a scale below that which is resolved by this reconstruction. In these processes, we can hypothesize a contribution from w_{uplift} in the nitrate upwelling since this component dominates the south of the eddy (Figure 11a). In this sense, the positive w in the upper part of D′ cast coincide with an area of uplifted isopy-

cnals (Figures 10 and 12) in the upper 50 m. This coincidence between the positive w and strong value of w_{uplift} is also present in the C cast suggesting its contribution to the restratification in contrast with w_{iso} (Figure 11) which results purely negative in our estimation.

Finally, while cast C′ is on the light side of the front, it is notable that the Lagrangian trajectory does not connect cast C to cast C′ within 24 hr. Instead, the deeper portions of cast C′ are located within the high salinity filament on the $\sigma = 28.0$ surface generated by along isopycnal subduction of Mediterranean water and in a region of net downward motion. We find conditions reflective of the Mediterranean water mass, which has low nutrient concentration down to 100 m (e.g., cast D). Here, along isopycnal stirring and w_{iso} in particular, result in the subduction of low nutrient surface water to depth.

6. Conclusion

Variational analysis, constrained by thermal wind, preserves fine-scale features in reconstructing density from a high-resolution ship survey. We highlighted the benefit of multivariate VA by adding terms to the cost function, which are based on the physical relations between variables instead of their a priori correlation as in OI. Constraints can be tailored to suit different available observations. In our case, we successfully combined the observed horizontal velocity along the front from ADCP measurements with the across-front hydrographic observations from the UCTD. Thus, the sharp density gradients at this intense front were preserved in both shape and magnitude, which allowed us to estimate considerable w through QG and SG omega equations. At the front, we obtained SG w up to 35 m/day, while QG w reached 20 m/day. Compared to the other reconstructions, the pattern of w from the multivariate VA, especially SG, produced more coherent downwelling (upwelling) on the dense (light) side of the front.

We separated w into isopycnal and uplift components. QG underestimates w_{iso}, which is 60% of the total w at the front. The importance of w_{iso} was confirmed by an analysis based on the projection of $\mathbf{u}_{\text{div}}$ on an isopycnal surface. The cumulative effect of the estimated w was highlighted by 3D particle advection, where the downwelling on the dense side of the front was 15 m/day. The downwelling particles closely followed isopycnals, confirming the importance of w_{iso}. The strongest downwelling (upwelling) is further confirmed by mapping drifter velocities, which reveals a surface convergence (divergence) at these locations. Our combination of Eulerian and Lagrangian techniques should be considered for future studies incorporating the deployment of large numbers of drifters. The trajectories of virtual particles agreed well with the observed vertical distribution of the nutrients. In the context of understanding the displacement of biochemical properties from the upper layer to the ocean interior, to the best of our knowledge, our work is the first study matching results from multi-platform observations to show the importance of along-isopycnal motion from in situ data. These submesoscale phenomena are frequently observed along the periphery mesoscale features in the Alboran Sea and elsewhere.

Future work could entail using the methods of this study to quantitatively update the subduction of carbon, nutrients, and other tracers. For future experiments in the western Mediterranean, we would recommend repeated surveys and a multi-platform approach to resolve the spatio-temporal variability of the unbalanced motions with the final aim of disentangling the different components of ageostrophic processes. Finally, we would like to stress how both process and general circulation ocean models could help to explore the capabilities of the developed thermal-wind constraint and explore further possibilities given by machine-learning techniques. In this sense, observing system simulation experiments can highlight the best way to deal with global observations such as Lagrangian float and large drifter deployments in order to improve the representation of ocean fronts. These new studies should also consider the high-resolution data provided by the upcoming SWOT satellite. The combination, through variational techniques, of remote sensing and in situ data could provide an improved reconstruction of the global state of the ocean.

Appendix A: Parameter Estimation

All the analysis we made, starting from the Optimal Interpolation to the VA mapping, requires a set of correlation lengths. As mentioned in Section 2, the horizontal coordinates were rotated to coincide with the across- and along-front directions (X and Y respectively). Based on the track of the R/V *Pourquoi Pas ?* (Figure 2), the across-front direction is densely sampled at 1-km resolution. The along-front separation is about 17 km. Thus the

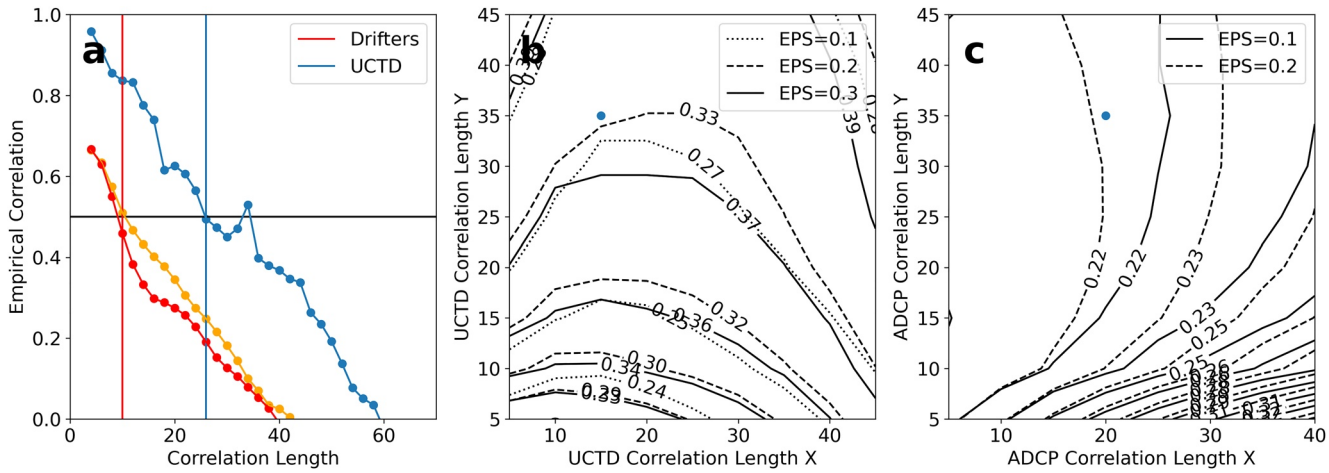

Figure A1. (a) The empirical correlation estimated with underway conductivity temperature depth system (UCTD) data and with the drifters data. (b) The root-mean-squared difference (RMSD) for the crossvalidation made with UCTD observations. (c) The RMSD for the crossvalidation made with the acoustic doppler current profiler observations.

Nyquist length is about 2 km (35 km) along (across) the front. Consequently, we have an important lower limit for the correlation length in Y.

We obtained a first estimation of the correlation lengths fitting a Gaussian-shaped function in the plot, which shows the correlation coefficient versus the observations distances Section Appendix A. As the literature suggests (Gomis et al., 2001), we select the values corresponding to full width half maximum-namely 10 km for drifters velocity and 25 km for the UCTD data.

Besides these initial estimates, the core method used to define the rest of the parameters and refine the correlation lengths consists of what is usually called cross-validation. Iteratively, all values in the parameters space were used to perform the analysis, withholding 30% of the data (Figure A1). We then compute the root-mean-squared difference (RMSD) between these excluded data and the reconstructed field for all the possible parameter combinations. The pair of the horizontal correlation lengths, finally selected for the UCTD analysis, are 15 and 35 km, while, for the ADCP, they are 20 and 35 km. The results of the cross-validation are presented in Section Appendix A there. In both ADCP and UCTD, we show how the representative error 0.1 and 0.2 lead to similar RMSD, so we selected a mean value of 0.15. Similarly, the vertical correlation length does not significantly affect the analyses, so we select 4 m.

A similar cross-validation procedure was conducted to select the weight of the multivariate constraint. As shown in Figure A2, activating the constraint, the RMSD with the UCTD validation samples actually increases a little.

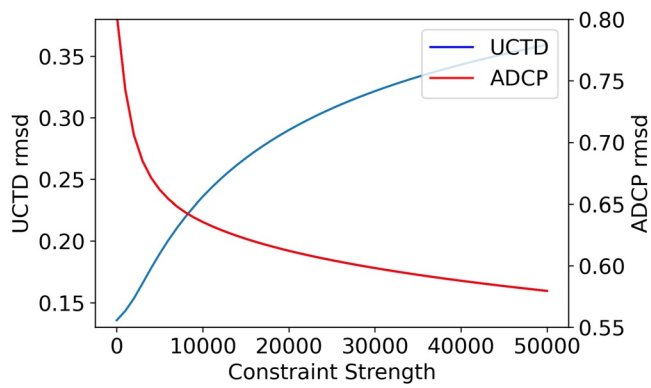

Figure A2. Root-mean-squared difference between the reconstruction and the underway conductivity temperature depth system (acoustic doppler current profiler) observations showed by the blue (red) line with the left (right) y-scale in comparison with the constrain strength.

At the same time, the RMSD with the ADCP rotational velocity decreases. A good compromise is found in the intersection of the two curves.

Data Availability Statement

The altimeter products were produced and distributed by Copernicus Marine Environmental Monitoring Service (https://resources.marine.copernicus.eu/product-detail/SEALEVEL_MED_PHY_L4_REP_OBSERVATIONS_008_051/INFORMATION). The rest of the data has DOI: https://doi.org/10.5281/zenodo.7216689.

Acknowledgments
This research was supported by the Office of Naval Research Departmental Research Initiative CALYPSO under program officers Terri Paluszkiewicz and Scott Harper. The authors' ONR Grant are as follows: N000141613130 (AP, SR and AM), N000141812418 (PMP), S. Johnston N000141812416 (TMSJ), N000141812138 (TO), N000141712517 and N00014191269 (LRC), N000141812139 and N000141812420 (AS) and N0000141812139and (EDA). Measurements were conducted from the R/V Pourquoi Pas? We are grateful to the captain and crew and the technical and scientific staff from all the institutions involved in making measurements. E. C. acknowledges support from the Spanish Ministerio de Ciencia e Innovacion (Grant BES-2017-080763). This article is also a contribution to the PRE-SWOT project funded by the Spanish Research Agency and the European Regional Development Fund (AEI/FEDER, UE) under grant agreement (CTM2016-78607-P).

References

Allen, J. T., Smeed, D. A., Tintoré, J., & Ruiz, S. (2001). Mesoscale subduction at the Almeria–Oran front: Part 1: Ageostrophic flow. *Journal of Marine Systems*, *30*(3), 263–285. https://doi.org/10.1016/S0924-7963(01)00062-8

Barth, A., Beckers, J.-M., Troupin, C., Alvera-Azcárate, A., & Vandenbulcke, L. (2014). Divand-1.0: -Dimensional variational data analysis for ocean observations. *Geoscientific Model Development*, *7*(1), 225–241. https://doi.org/10.5194/gmd-7-225-2014

D'Asaro, E. A. (2003). Performance of autonomous Lagrangian floats. *Journal of Atmospheric and Oceanic Technology*, *20*(6), 896–911. https://doi.org/10.1175/1520-0426(2003)020<0896:POALF>2.0.CO;2

Dawson, A. (2016). Windspharm: A high-level library for global wind field computations using spherical harmonics. *Journal of Open Research Software*, *4*(1), e31. https://doi.org/10.5334/jors.129

Delandmeter, P., & van Sebille, E. (2019). The parcels v2.0 Lagrangian framework: New field interpolation schemes. *Geoscientific Model Development*, *12*(8), 3571–3584. https://doi.org/10.5194/gmd-12-3571-2019

Dobricic, S., & Pinardi, N. (2008). An oceanographic three-dimensional variational data assimilation scheme. *Ocean Modelling*, *22*(3), 89–105. https://doi.org/10.1016/j.ocemod.2008.01.004

Donlon, C. J., Martin, M., Stark, J., Roberts-Jones, J., Fiedler, E., & Wimmer, W. (2012). The operational sea surface temperature and sea ice analysis (OSTIA) system. *Remote Sensing of Environment*, *116*, 140–158. https://doi.org/10.1016/j.rse.2010.10.017

Escudier, R., Renault, L., Pascual, A., Brasseur, P., Chelton, D., & Beuvier, J. (2016). Eddy properties in the Western Mediterranean Sea from satellite altimetry and a numerical simulation. *Journal of Geophysical Research: Oceans*, *121*(6), 3990–4006. https://doi.org/10.1002/2015JC011371

Esposito, G., Berta, M., Centurioni, L., Johnston, T. S., Lodise, J., Özgökmen, T., et al. (2021). Submesoscale vorticity and divergence in the Alboran Sea: Scale and depth dependence. *Frontiers in Marine Science*, *8*, 678304. https://doi.org/10.3389/fmars.2021.678304

Freilich, M. A., & Mahadevan, A. (2019). Decomposition of vertical velocity for nutrient transport in the upper ocean. *Journal of Physical Oceanography*, *49*(6), 1561–1575. https://doi.org/10.1175/JPO-D-19-0002.1

Gent, P. R., McWilliams, J. C., & Snyder, C. (1994). Scaling analysis of curved fronts. Validity of the balance equations and semigeostrophy. *Journal of the Atmospheric Sciences*, *51*(1), 160–163. https://doi.org/10.1175/1520-0469(1994)051<0160:SAOCFV>2.0.CO;2

Gomis, D., Ruiz, S., & Pedder, M. A. (2001). Diagnostic analysis of the 3D ageostrophic circulation from a multivariate spatial interpolation of CTD and ADCP data. *Deep Sea Research Part I: Oceanographic Research Papers*, *48*(1), 269–295. https://doi.org/10.1016/S0967-0637(00)00060-1

Guinehut, S., Larnicol, G., & Le Traon, P. Y. (2002). Design of an array of profiling floats in the north Atlantic from model simulations. *Journal of Marine Systems*, *35*(1), 1–9. https://doi.org/10.1016/S0924-7963(02)00042-8

Halliwell, G. R., Srinivasan, A., Kourafalou, V., Yang, H., Willey, D., Le Hénaff, M., & Atlas, R. (2014). Rigorous evaluation of a fraternal twin ocean OSSE system for the open gulf of Mexico. *Journal of Atmospheric and Oceanic Technology*, *31*(1), 105–130. https://doi.org/10.1175/JTECH-D-13-00011.1

Hoskins, B. J., & Draghici, I. (1977). The forcing of ageostrophic motion according to the semi-geostrophic equations and in an isentropic coordinate model. *Journal of the Atmospheric Sciences*, *34*(12), 1859–1867. https://doi.org/10.1175/1520-0469(1977)034<1859:TFOAMA>2.0.CO;2

Hoskins, B. J., Draghici, I., & Davies, H. C. (1978). A new look at the ω-equation. *Quarterly Journal of the Royal Meteorological Society*, *104*(439), 31–38. https://doi.org/10.1002/qj.49710443903

Ioannou, A., Stegner, A., Tuel, A., Levu, B., Dumas, F., & Sabrina, S. (2019). Cyclostrophic corrections of AVISO/DUACS surface velocities and its application to mesoscale eddies in the Mediterranean Sea.

Iudicone, D., Rodgers, K., Stendardo, I., Aumont, O., Madec, G., Bopp, L., et al. (2011). Water masses as a unifying framework for understanding the southern ocean carbon cycle. *Biogeosciences*, *8*(5), 1031–1052. https://doi.org/10.5194/bg-8-1031-2011

Johnston, T. M. S., Rudnick, D. L., & Pallàs-Sanz, E. (2011). Elevated mixing at a front. *Journal of Geophysical Research*, *116*(C11). https://doi.org/10.1029/2011JC007192

Klein, P., & Lapeyre, G. (2009). The oceanic vertical pump induced by mesoscale and submesoscale turbulence. *Annual Review of Marine Science*, *1*(1), 351–375. https://doi.org/10.1146/annurev.marine.010908.163704

Le Traon, P. Y., & Morrow, R. (2001). Chapter 3 ocean currents and eddies. In L.-L. Fu & A. Cazenave (Eds.), *International Geophysics*. (Vol. 69, pp. 171). Academic Press. https://doi.org/10.1016/S0074-6142(01)80148-0

Liszka, T., & Orkisz, J. (1980). The finite difference method at arbitrary irregular grids and its application in applied mechanics. *Computers & Structures*, *11*(1), 83–95. https://doi.org/10.1016/0045-7949(80)90149-2

Liu, Y., & Weisberg, R. (2011). Evaluation of trajectory modeling in different dynamic regions using normalized cumulative Lagrangian separation. *Journal of Geophysical Research*, *116*(C9), C09013. https://doi.org/10.1029/2010JC006837

Lodise, J., Özgökmen, T., Gonçalves, R. C., Iskandarani, M., Lund, B., Horstmann, J., et al. (2020). Investigating the formation of submesoscale structures along mesoscale fronts and estimating kinematic quantities using Lagrangian drifters. *Fluids*, *5*(3), 159. https://doi.org/10.3390/fluids5030159

Mahadevan, A., D'Asaro, E. A., Allen, J. T., Almaraz García, P., Alou-Font, E., Aravind, H. M., et al. (2019). *CALYPSO 2019 cruise report: Field campaign in the mediterranean (technical report)*. Woods Hole Oceanographic Institution. https://doi.org/10.1575/1912/25266

Mahadevan, A., & Tandon, A. (2006). An analysis of mechanisms for submesoscale vertical motion at ocean fronts. *Ocean Modelling*, *14*(3), 241–256. https://doi.org/10.1016/j.ocemod.2006.05.006

Mahadevan, A., Pascual, A., Rudnick, D. L., Ruiz, S., Tintoré, J., & D'Asaro, E. (2020). Coherent pathways for vertical transport from the surface ocean to interior. *Bulletin of the American Meteorological Society*, *101*(11), E1996–E2004. https://doi.org/10.1175/BAMS-D-19-0305.1

McWilliams, J. C. (2019). A survey of submesoscale currents. *Geoscience Letters*, *6*(1), 3. https://doi.org/10.1186/s40562-019-0133-3

Morrow, R., Fu, L.-L., Ardhuin, F., Benkiran, M., Chapron, B., Cosme, E., et al. (2019). Global observations of fine-scale ocean surface topography with the surface water and ocean topography (SWOT) mission. *Frontiers in Marine Science*, *6*. https://doi.org/10.3389/fmars.2019.00232

Nardelli, B. B., Mulet, S., & Iudicone, D. (2018). Three-dimensional ageostrophic motion and water mass subduction in the southern ocean. *Journal of Geophysical Research: Oceans*, *123*(2), 1533–1562. https://doi.org/10.1002/2017JC013316

Niiler, P. (2001). Chapter 4.1 the world ocean surface circulation. In G. Siedler, J. Church, & J. Gould (Eds.), *International Geophysics*. (Vol. 77, pp. 193–204). Academic Press. https://doi.org/10.1016/S0074-6142(01)80119-4

Pallàs-Sanz, E., Johnston, T., & Rudnick, D. (2010). Frontal dynamics in a California current system shallow front: 2. Mesoscale vertical velocity. *Journal of Geophysical Research*, *115*(C12). https://doi.org/10.1029/2010JC006474

Pascual, A., Ruiz, S., Olita, A., Troupin, C., Claret, M., Casas, B., et al. (2017). A multiplatform experiment to unravel meso- and submesoscale processes in an intense front (AlborEx). *Frontiers in Marine Science*, *4*. https://doi.org/10.3389/fmars.2017.00039

Rabier, F., Järvinen, H., Klinker, E., Mahfouf, J.-F., & Simmons, A. (2000). The ECMWF operational implementation of four-dimensional variational assimilation. I: Experimental results with simplified physics. *Quarterly Journal of the Royal Meteorological Society*, *126*(564), 1143–1170. https://doi.org/10.1002/qj.49712656415

Rosso, I., Hogg, A. M., Strutton, P. G., Kiss, A. E., Matear, R., Klocker, A., & van Sebille, E. (2014). Vertical transport in the ocean due to sub-mesoscale structures: Impacts in the kerguelen region. *Ocean Modelling*, *80*, 10–23. https://doi.org/10.1016/j.ocemod.2014.05.001

Rudnick, D. L. (1996). Intensive surveys of the azores front: 2. Inferring the geostrophic and vertical velocity fields. *Journal of Geophysical Research*, *101*(C7), 16291–16303. https://doi.org/10.1029/96JC01144

Rudnick, D. L., & Klinke, J. (2007). The underway conductivity–temperature–depth instrument. *Journal of Atmospheric and Oceanic Technology*, *24*(11), 1910–1923. https://doi.org/10.1175/JTECH2100.1

Rudnick, D. L., Zarokanellos, N. D., & Tintoré, J. (2022). A four-dimensional survey of the almeria–oran front by underwater gliders: Tracers and circulation. *Journal of Physical Oceanography*, *52*(2), 225–242. https://doi.org/10.1175/JPO-D-21-0181.1

Ruiz, S., Claret, M., Pascual, A., Olita, A., Troupin, C., Capet, A., et al. (2019). Effects of oceanic mesoscale and submesoscale frontal processes on the vertical transport of phytoplankton. *Journal of Geophysical Research: Oceans*, *124*(8), 5999–6014. https://doi.org/10.1029/2019JC015034

Ruiz, S., Pascual, A., Garau, B., Pujol, I., & Tintoré, J. (2009). Vertical motion in the upper ocean from glider and altimetry data. *Geophysical Research Letters*, *36*(14), L14607. https://doi.org/10.1029/2009GL038569

Shakespeare, C. J., Gibson, A. H., Hogg, A. M., Bachman, S. D., Keating, S. R., & Velzeboer, N. (2021). A new open source implementation of Lagrangian filtering: A method to identify internal waves in high-resolution simulations. *Journal of Advances in Modeling Earth Systems*, *13*(10), e2021MS002616. https://doi.org/10.1029/2021MS002616

Tarry, D. R., Essink, S., Pascual, A., Ruiz, S., Poulain, P.-M., Özgökmen, T., et al. (2021). Frontal convergence and vertical velocity measured by drifters in the alboran sea. *Journal of Geophysical Research: Oceans*, *126*(4), e2020JC016614. https://doi.org/10.1029/2020JC016614

Tintoré, J., Gomis, D., Alonso, S., & Parrilla, G. (1991). Mesoscale dynamics and vertical motion in the alborán sea. *Journal of Physical Oceanography*, *21*(6), 811–823. https://doi.org/10.1175/1520-0485(1991)021<0811:MDAVMI>2.0.CO;2

Viudez, A., & Dritschel, D. (2004). Potential vorticity and the quasigeostrophic and semigeostrophic mesoscaleVertical velocity. *Journal of Physical Oceanography*, *34*(4), 865–887. https://doi.org/10.1175/1520-0485(2004)034<0865:PVATQA>2.0.CO;2

Viúdez, Á., Tintoré, J., & Haney, R. L. (1996). Circulation in the Alboran Sea as determined by quasi-synoptic hydrographic observations. Part I: Three-dimensional structure of the two anticyclonic gyres. *Journal of Physical Oceanography*, *26*(5), 684–705. https://doi.org/10.1175/1520-0485(1996)026<0684:CITASA>2.0.CO;2

Wang, Y., & Luo, Y. (2020). Variability of spice injection in the upper ocean of the southeastern Pacific during 1992–2016. *Climate Dynamics*, *54*(5), 3185–3200. https://doi.org/10.1007/s00382-020-05164-y

Zarokanellos, N. D., Rudnick, D. L., Garcia-Jove, M., Mourre, B., Ruiz, S., Pascual, A., & Tintoré, J. (2022). Frontal dynamics in the Alboran Sea: 1. Coherent 3D Pathways at the almeria-oran front using underwater glider observations. *Journal of Geophysical Research: Oceans*, *127*(3), e2021JC017405. https://doi.org/10.1029/2021JC017405